EVLA Memo #205

VLA polarization calibration: RL phase stability

Frank K. Schinzel (NRAO)

May 2, 2018

Contents

1 Context

The VLA sky survey uses the EVLA S-band receiver (2.0–4.0 GHz) and aims to provide polarization calibrated data for the primary purpose of rotation measure synthesis. For VLASS the requirements are summarized in VLASS Project Memo #3 as defined by the VLA Survey Science group and were further refined in the VLASS system requirements document (SCI-BDP-022). The survey description and science case states that the survey be sensitive to polarized instensities >1.5 mJy beam^{-1} and provide a rotation measure precision of better than 5 rad m^{-2}. There is no mention of a required absolute polarization angle accuracy. The VLASS systems requirements document states a requirement that "The linear polarization angle calibration shall be better than 2° over 90% of the observed area". In addition, the polariztion leakage requirement is at <0.75% over 90% of the survey, with a goal of 0.25%. The characterization of polarization leakage and rotation measure calibration limits are not part of the discussion in this document.

The general VLASS polarization observing and calibration strategy is as follows:

- The residual delay between the parallel hands, i.e. the cross-hand delay, is determined from one scan of 3C 286 or 3C 48. In the case of 3C 48, due to its low fractional polarization around 3.0 GHz, one of the two calibrators J1800+7828 or 3C 138 is observed alongside 3C 48 as alternate calibrator.

- The instrumental polarization terms are solved with per channel resolution (2 MHz) using either a polarized source with at least 60° parallactic angle coverage and solving for its QU term together with the instrumental polarization (Df+QU) or using a known unpolarized source (Df).

- The absolute polarization angle is determined based on full Stokes point source models of 3C 286, J1800+7828, or 3C 138 solving for the RL/LR phase with a per channel resolution of 2 MHz.

A more detailed description on the principels of interferometric polarimetric calibration can be found in Sault & Perley (2014) [1].

2 Verification of Calibration - Pointed Tests

To verify the accuracy of the polarization calibration in the context of VLASS three datasets were used, listed in Table 1. The TCAL0004 observations contain a larger number of primary and secondary flux density calibrators including frequent observations of 3C 48, 3C 138, 3C 286, and J1800+7828. In addition, a choice of polarized Northern sources with good parallactic angle coverage are also included which can be used to determine the instrumental polarization. The TSKY0001 dataset had the particular purpose to observe 3C 286 through transit (hour angles -2.0 to 2.0 hours). This dataset also includes an unpolarized source OQ208 and a weakly polarized calibrator J1327+2210 that were frequently observed along with 3C 286.

Table 1: Verification test datasets.

Date	Project	sbid	Config.	Bands
2014-02-16/17	TCAL0004	28851845	A	P,L,S,C,X,U,K,Ka,Q
2014-10-11/12	TCAL0004	29746293	C	4,P,L,S,C,X,U,K,Ka,Q
2016-09-11	TSKY0001	32712864	B	L,S,X

2.1 Calibration

The datasets were manually calibrated both using CASA and AIPS for comparability purposes. In the case of CASA, version 5.1.1-5 was used, in the case of AIPS, version 31DEC18 was used.

2.1.1 CASA

The calibration followed standard procedure with the following general steps:

1. Import from SDM $\Rightarrow$ split out bands $\Rightarrow$ split out single spectral window to be calibrated

2. Parallel-hand calibration:
   - setjy with appropriate model for parallel hands
   - gaincurve, requantizer gains, antenna position corrections, TEC optionally
   - determine delay offsets (gaincal gaintype='K' on single scan of 3C 286)
   - phase calibration and solving for bandpass on single scan of 3C 286
   - phase and amplitude&phase calibration on all targets

3. Cross-hand calibration:
   - Reset setjy with appropriate model for cross-hands (full polarization model of 3C 286)
   - cross-hand delay determination for reference antenna on single scan of 3C 286
   - determine instrumental polarization (Df+QU) with 2 MHz channels
   - cross-hand phase correction with 2 MHz channels on single scan

4. Apply derived calibration tables with parallactic angle correction

2.1.2 AIPS

The calibration followed closely that of the CASA calibration with only small AIPS specific differences. In the following the order of main tasks that were run are listed.

1. Loading data:
   - import BDF2AIPS
   - TYAPL to apply requantizer gains
   - SPLAT to split out single IF
   - VLANT apply antenna position offsets
2. Parallel-hand calibration:
   - SETJY with appropriate model for 3C 286
   - FRING delay only solutions on single scan
   - CALIB with solmode 'P' and BPASS
   - CALIB with solmode 'P' and 'A&P' and flux scaling (GETJY)
3. Cross-hand calibration:
   - RLDLY on single scan
   - PCAL/RLDIF coarse ⇒ PCAL/RLDIF spectrally (2 MHz) on single scan

3 Results

Following the above described calibration procedure using CASA and the A array TCAL0004 dataset, the resulting calibrated cross-hand phases (RL) are plotted for the three targets 3C 286, J1800+7828, and 3C 138 in Fig. 1. Each data point is averaged across a single RFI free spectral window within the lower baseband of the S-band part of the observation, and averaged per scan in time, and across all baselines. Only the scan of 3C 286 around -3.0 h was used for polarization calibration.

A number of observations can made from Fig. 1:

- For a perfectly calibrated dataset we expect very little variation in RL phase over time. However, we see significant variation in the cross-hand phase for all three targets plotted.
- There is a discontinuity right around 0 hour angle of 3C 286.
- In 3C 286 the RL phase is more or less stable over time before transit, while values post-transit settle around 4° off in phase from pre-transit. In the case of 3C 138 the phases slowly change from around 77° to 71° while transiting, whereas J1800+7828 shows a sinusoidal behavior showing a phase variation of about 7°.

- The magnitude of the RL phase variation is independent of source declination, however each of the calibrators exhibit a distinct RL phase variation.

Overall, the phase variations that are seen translate to an uncertainty in absolute polarization angle of about $2° - 4°$, which clearly does not fulfill the VLASS requirement of $2°$ or better. The discontinuity for the transit of 3C 286 has been observed in the past and is related to 3C 286 passing close to local zenith and antenna pointing. However, the variations seen before and after transit, as well as for 3C 138 and J1800+7828 have a residual geometric signature that aligns with changes in parallactic angle and are not removed through calibration. In addition, in the case of 3C 286 a post-transit gradual increase in RL phase by about $1°$ is observed between 2.0 and 6.0 h, which coincides with sunrise and could be due to changes in the ionosphere at that time. In the following, potential causes of this observed RL phase variability are investigated.

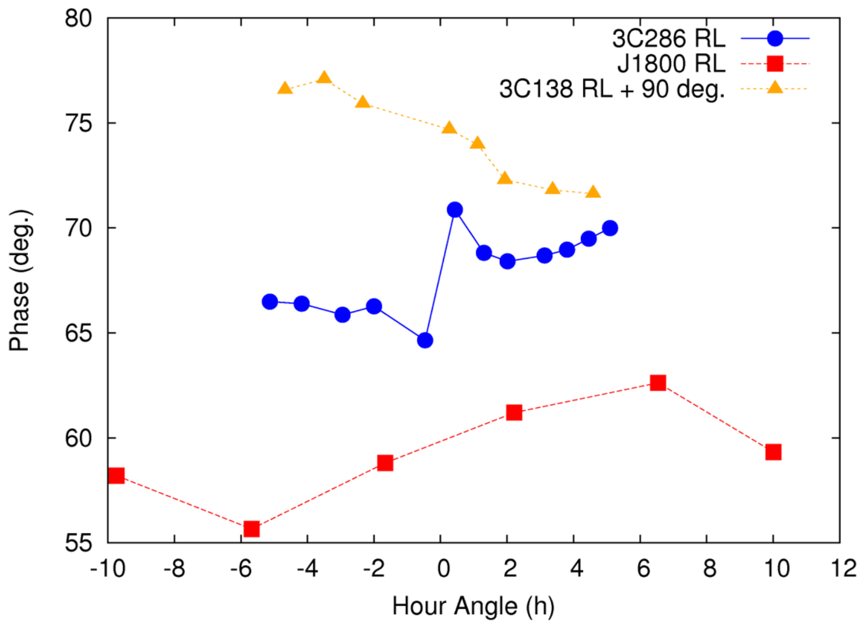

Figure 1: RL phase against hour angle for three select targets 3C 286, 3C 138, and J1800+7828. Note that the phase values for 3C 138 had $90°$ added for better visibility.

3.1 Influence of the Ionosphere

The A-array TCAL0004 dataset was observed half throughout the night with the second half passing through sunrise and charging of the ionosphere. The C-array TCAL0004 dataset was observed similarly to the A-array one, however due to shorter baselines the ionosphere plays a lesser role. The TSKY0001 dataset was observed exculsively during daytime with a charged ionosphere, however the overall total electron content (TEC) variation of the ionosphere during the observation was small, the dominating effect from the ionosphere was primarily elevation dependence and the change of the volume element the radio signals pass through. The changes in (TEC) units over time for two of the three observations are visualized in Fig. 2, the TCAL0004 C-array dataset failed processing through the CASA TEC correction task, which cause is being investigated at the time of writing of this document.

The maximum likely effect of the ionosphere for a source observed at 3.0 GHz and a zenith angle of 60° is about 3.1° in angle and about 17 ns in group delay, during night time these are a factor of 10 lower. The values were derived for a value of 50 TECU during the day and 5 TECU at night [2]. Thus, absolute polarization angle calibration can still be significantly affected by ionospheric variations over the course of an observation. However, since the absolute angle calibration is performed at a particular TECU and orientiation to Earth's magnetic field lines, the effect is expected to be smaller for typical S-band VLA observations, where the difference in TECU and magnetic field direction dominates the errors introduced into the absolute polarization angle calibration due to the ionosphere. During VLASS1.1 observations the median projected variation in TECU for all observations was 12 TECU, with a minimum of 1.6 and a maximum of 75 TECU, which corresponds to introduced errors due to a maximum ionospheric Faraday rotation of $\sim$1° for the median and for the full range of observed changes in the delta TECU of 0.1° – 4.6°.

In TCAL0004 A-array data, the ΔTECU before sunrise is about 16 TECU, while the change from night to day introduced a change by a factor of 10. This corresponds to a maximum relative error in absolute polarization angle of up to $\sim$1.3° during the night and a relative error of up to $\sim$3.1° during sunrise. Figure 3 illustrates that the last four data points in the RL phase plot of 3C 286 are most affected by the ionosphere and when attempting to correct for changes in the ionosphere the ionospheric Faraday rotation seems to be overcompensated, thus rotating the cross-hand phase in the opposite direction. Despite ionospheric Faraday rotation, the offset in phase before and after transit remains. The magnitude of the observed ionospheric Faraday rotation seems to contribute little error in phase during night time and only the last four data points show an increase by 1.5° in phase, while the observed phase difference before and after transit is a factor of 2 higher. Thus, **the observed change in cross-hand phase is not entirely explainable by ionospheric Faraday rotation**. Moreover, as will be shown in Sec. 3.4, the observed RL phase variability is also present at higher frequency X-band data, which is significantly less influenced by ionospheric effects.

3.2 Calibration CASA vs. AIPS

The TCAL0004 A-array dataset was calibrated both in CASA and AIPS following the steps outlined in Section 2.1. Fig. 4 plots the resulting RL phases for the three targets 3C 286, 3C 138, and J1800+7828. Similar trends are observed between CASA and AIPS calibration, despite some small offsets in derived values due to differences in data binning and slight

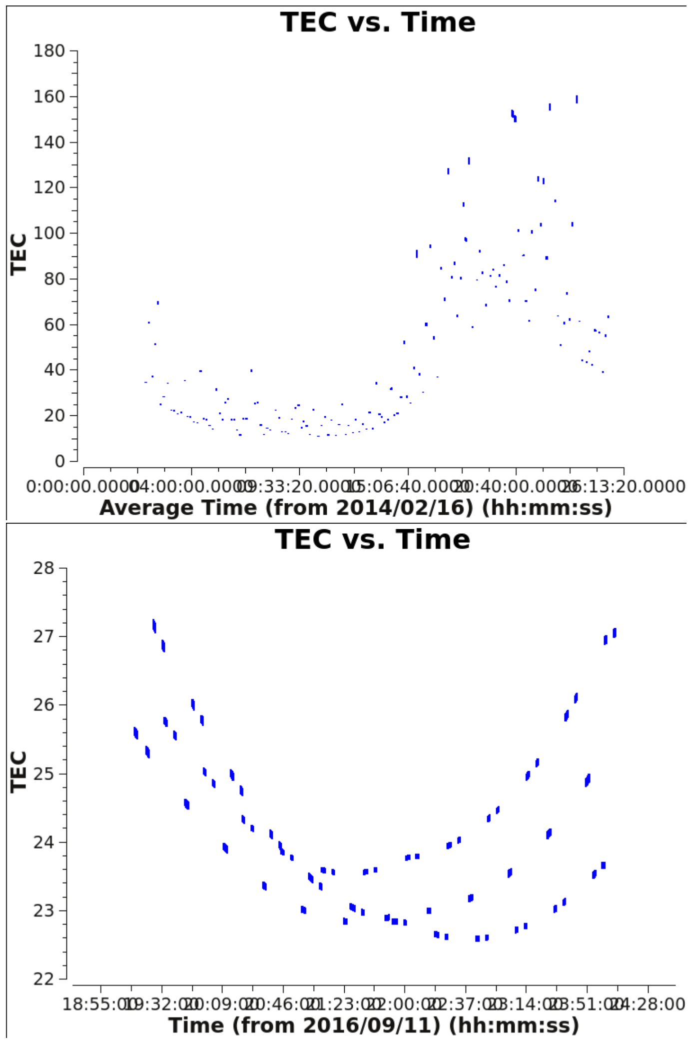

Figure 2: Projected total electron content unit (TECU) for S-band pointings of two of the three test datasets as derived through the standard ionospheric correction task in CASA. *Top:* TCAL0004 A-array; *Bottom:* TSKY0001 B-array.

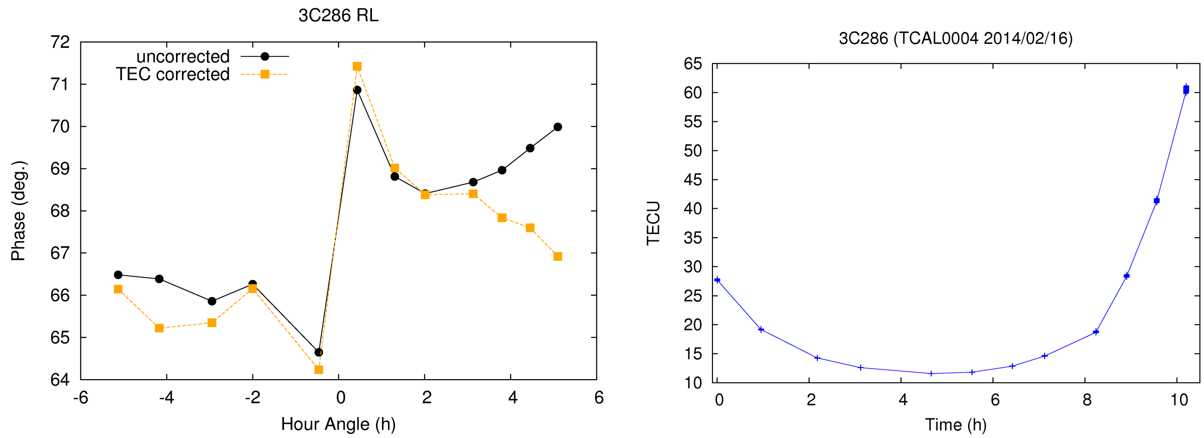

Figure 3: Left: RL phase of 3C 286 at S-band in TCAL0004 A-array dataset before and after TEC corrections were applied during calibration with CASA. Right: Change in projected TEC for corresponding scans.

differences how parallactic angles are calculated. However, overall we can conclude that the observed RL variability **does not depend on whether data is calibrated with AIPS or CASA**.

3.3 Array configurations

The RL phase against hour angle is derived for all three test datasets (see Sec. 2) representing primarily VLA A, B, and C array configurations. Fig. 5 shows the resulting RL phases plotted against hour angle and elevation for 3C 286, while Fig. 6 shows RL phases only plotted against hour angle for 3C 138 and J1800+7828. It is immediately evident that A and B array phases are in good agreement in the case of 3C 286; 3C 138 and J1800+7828 were not included in the B array dataset. However, C array data differs significantly but also shows RL phase variability that resembles an elevation dependence rather than a geometric/parallactic angle dependence.

3.4 S vs. X-band

Using the TSKY0001 B array dataset, RL phases were compared for both S and X band (single spectral window in lower baseband). Fig. 7 shows the obtained RL phases for 3C 286 at both bands. Comparisons shows **similar phase behavior at both S and X band**, while the magnitude of the effect is actually larger, 7° in phase in the case of X band and 5° in phase in the case of S band.

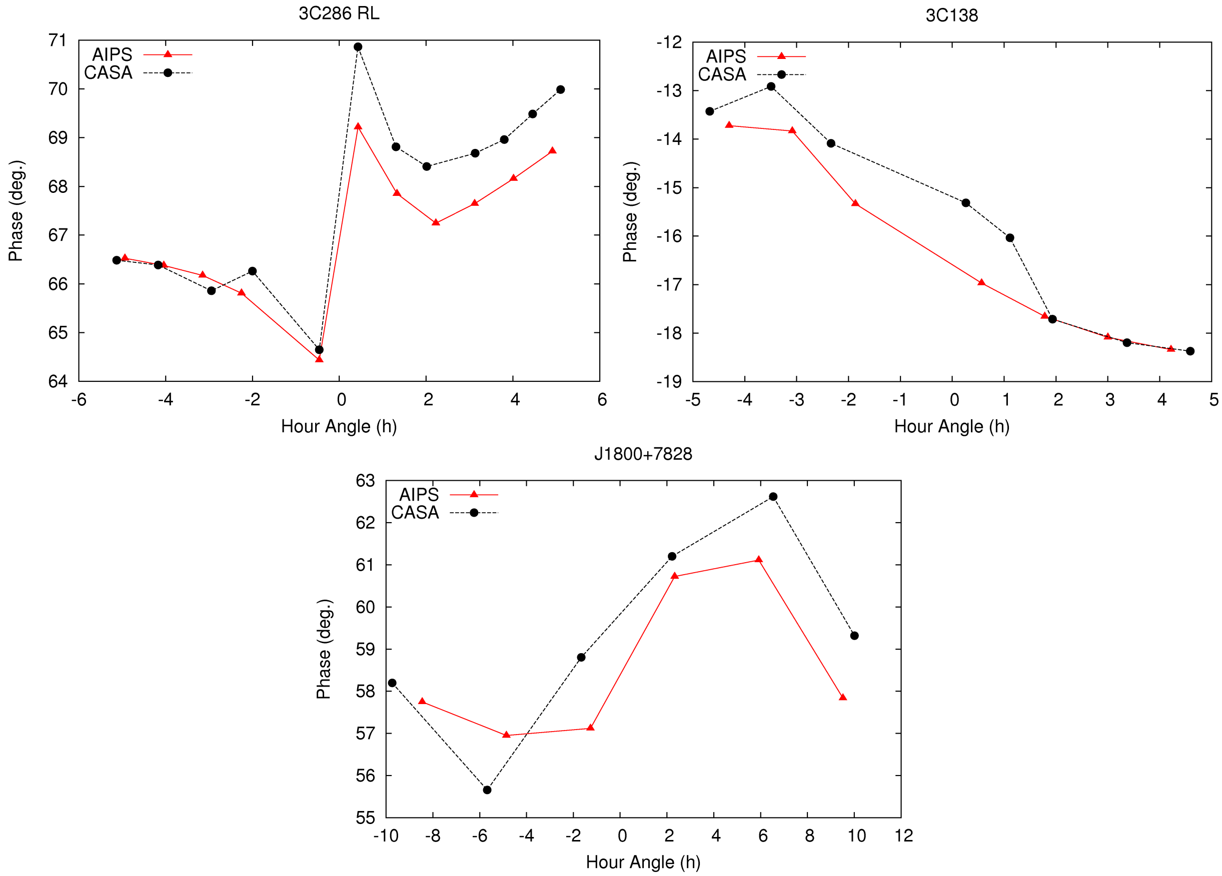

Figure 4: RL phase of 3C 286, 3C 138, and J1800+7828 derived from calibration with AIPS and CASA.

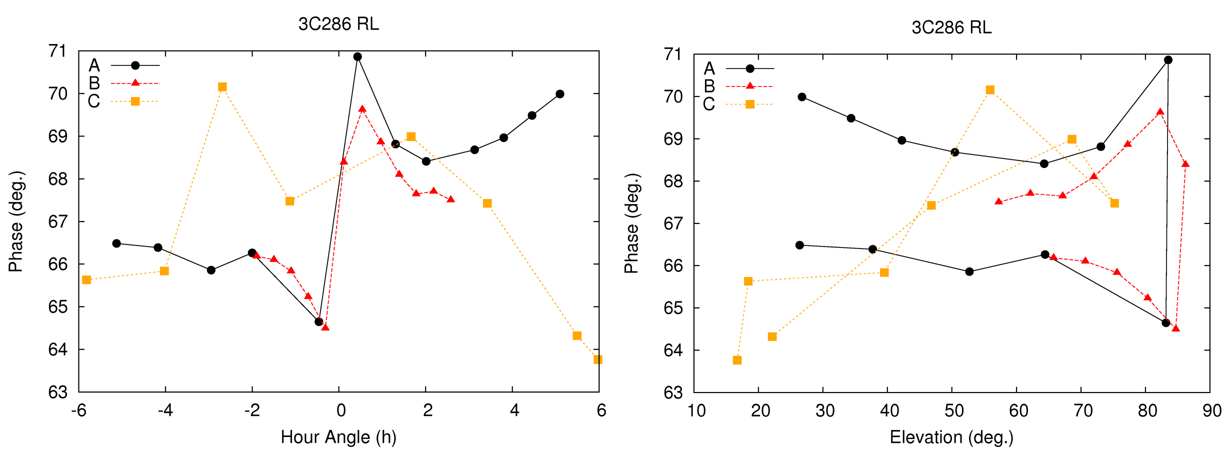

Figure 5: RL phase for 3C 286 plotted against hour angle (left) and elevation (right) for the three test datasets representing A, B, and C array configurations.

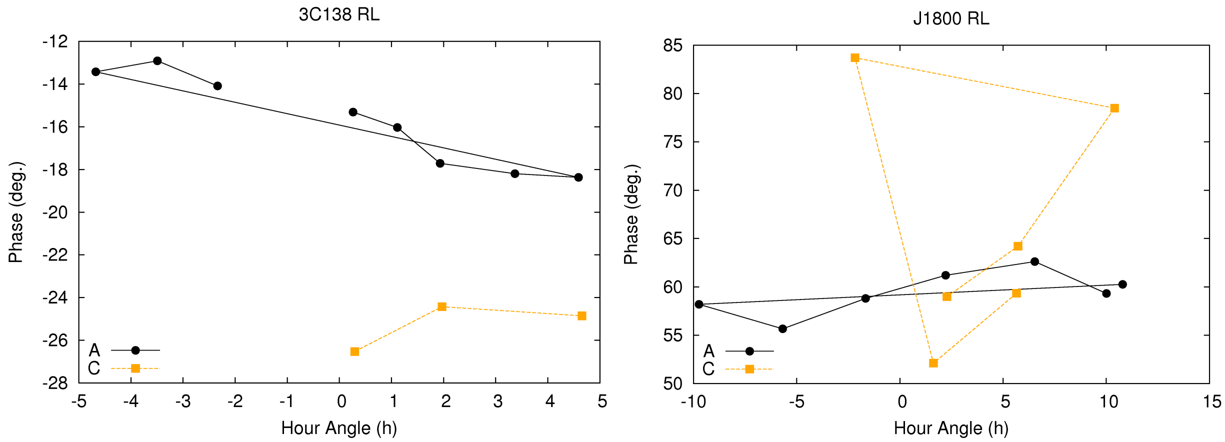

Figure 6: RL phase for 3C 138 (left) and J1800+7828 (right) plotted against hour angle for the two TCAL0004 datasets representing A and C array configurations.

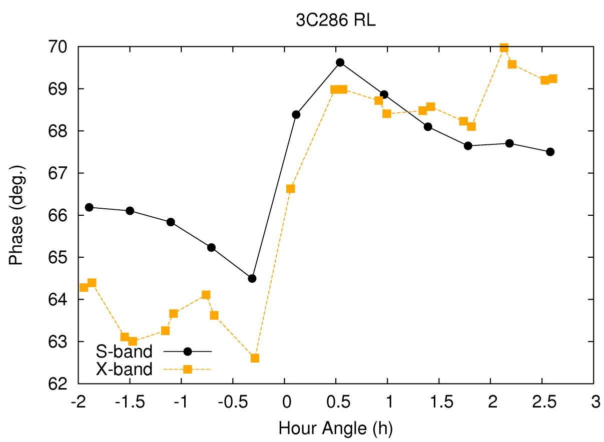

Figure 7: RL phase for 3C 286 plotted against hour angle for S and X band in B array configuration.

3.5 Source Structure

From each dataset, in particular from the most extended configurations, full Stokes images were derived which can be used for recalibration of the datasets. Example model images are shown in Figs. 8 and 9 for all three considered targets. In the case of 3C 286 there is polarized structure observed 2.5" South-West of the primary peak emission, which has a Stokes I peak flux of 58 mJy beam^{-1} and a polarized intensity of 20 mJy beam^{-1}. The peak flux of the primary emission component is 8.9 Jy with a polarized flux of 0.96 Jy. Thus, the polarized secondary structure corresponds to less than 2% of the polarized intensity of the main polarization component and 0.65% of the Stokes I flux. This component is not expected to be of significant influence, while the dominant polarized emission has a linear polarization angle of 33°, the secondary polarization structure seems to show a linear polarization angle of $\sim$90°. Given this, the combined error on the Q/U flux could add to an error of up to $\sim$1.3° in absolute polarization angle and would not have a significant influence on the observed RL phase variations. In the case of 3C 138 and J1800+7828 no significant polarized source structure was found.

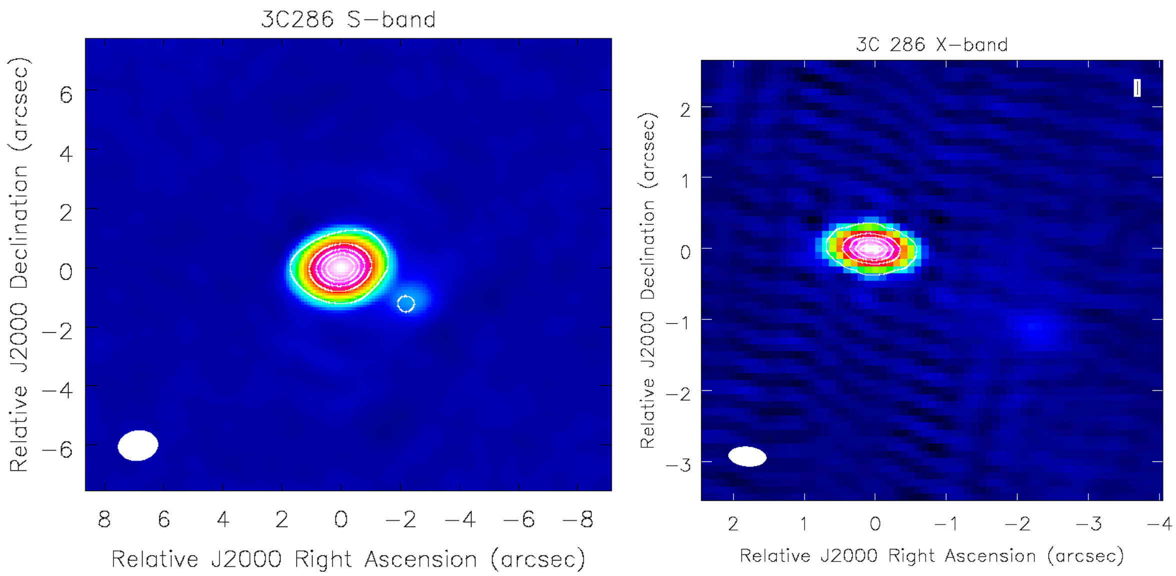

Figure 8: Images of 3C 286 at S band in A array configuration (left) and X band in B array configuration. The colorscale represents the spatial distribution of Stokes I flux, while the contours indicate the presence of polarized emission with the innermost contour representing a polarization fraction of $\sim$ 10%. The lowest contour level represents 2% of the peak polarized intensity.

To test the hypothesis that the secondary polarization component of 3C 286 can be neglected for polarization angle calibration, a full stokes point source model calibration is compared to calibration using the source model. Solutions were determined for each case using a single calibration scan (see Fig. 10) and in a second step solving for cross-hand

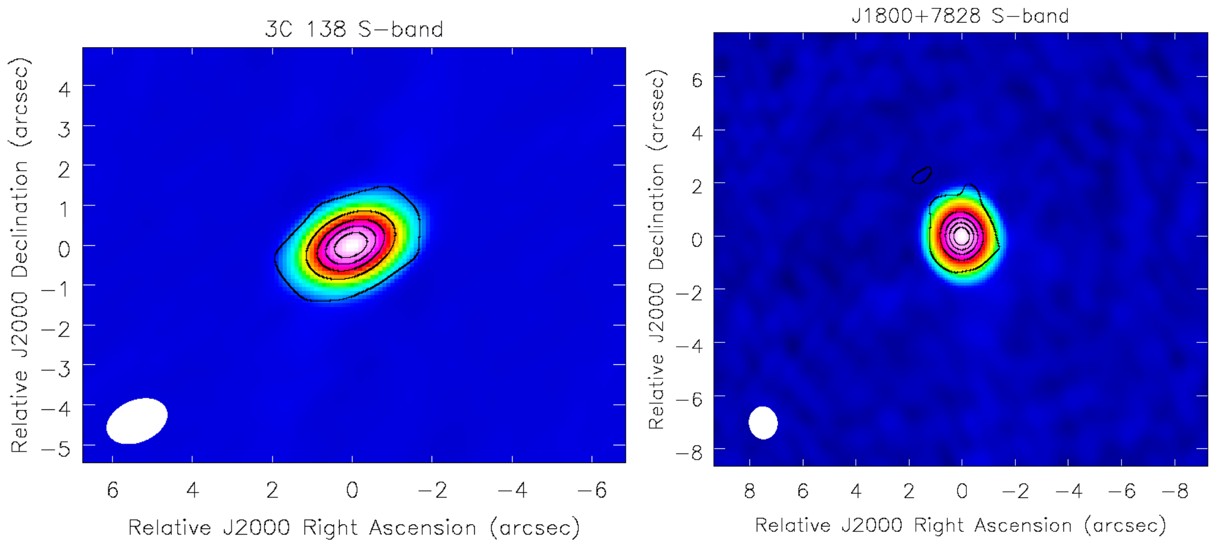

Figure 9: Images of 3C 138 (left) and J1800+7828 (right) at S band in A array configuration. The colorscale represents the spatial distribution of Stokes I flux, while the contours indicate the presence of polarized emission with the innermost contour representing the polarization fraction. The lowest contour level represents 2% of the peak polarized intensity.

phases using a point source model and using the model components (see Fig. 11). No significant difference is seen between applying a point source model or applying a model that accounts for polarized source structure when solving for RL phase. **The conclusion is that source structure seems not relevant in the context of observed RL phase variation.**

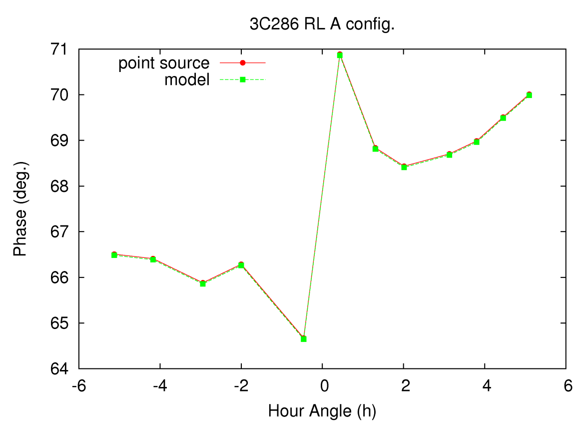

Figure 10: Resulting RL phases using a point source model (red) and model image (green) for determining the RL delay and phase offsets.

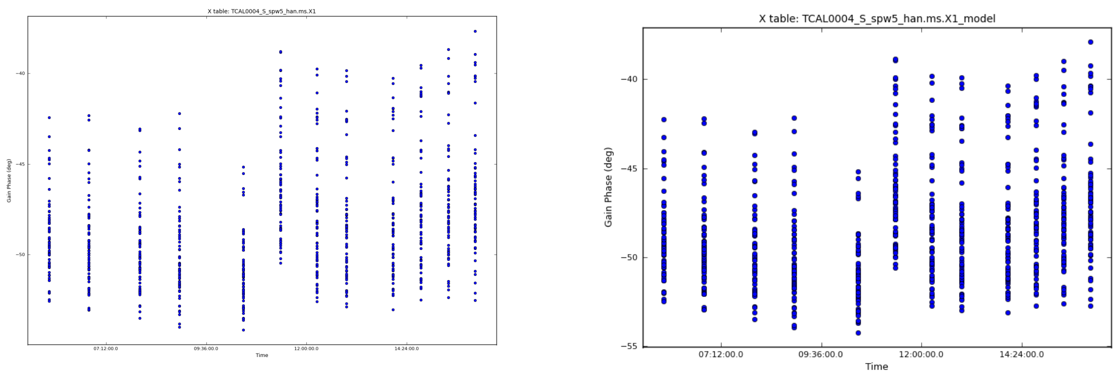

Figure 11: Calibration table phase solutions for RL phase when using a point source model (left) and when using a model image (right) and solving for each scan.

3.6 Instrumental Polarization

In the following the TSKY0001 dataset at X band is used to compare different methods deriving the per antenna instrumental polarization. Three different strategies were used:

1. The unpolarized calibrator OQ208 was used to solve for frequency dependent polarization structure with 2 MHz spectral resolution, i.e. not solving for source polarization (Df OQ208).

2. The weakly polarized calibrator J1327+2210 was used to solve for frequency dependent polarization structure with 2 MHz spectral resolution, while solving for source instrinsic polarization. The observations of J1327+2210 covered 60° on each side of transit, i.e. a total of 120° (Df+QU J1327+2210).

3. The strongly polarized calibrator 3C 286 was used to solve for frequency dependent polarization structure with 2 MHz spectral resolution, while solving for source intrinsic polarization. Parallactic angle coverage was $\sim 70°$ on either side of transit, i.e. a total of 140° (Df+QU 3C 286).

As can be seen in Fig. 12, there is little difference between the different ways from deriving the instrumental polarization. However, 3C 286 is not a good calibrator due to its strong polarization ∼10% and high flux density. Despite this, the RL phase variation is seen as well. Overall there is **no significant difference in observed RL phases between using an unpolarized calibrator (not solving for Q/U) and a polarized calibrator (solving for Q/U) for deriving instrumental polarization.**

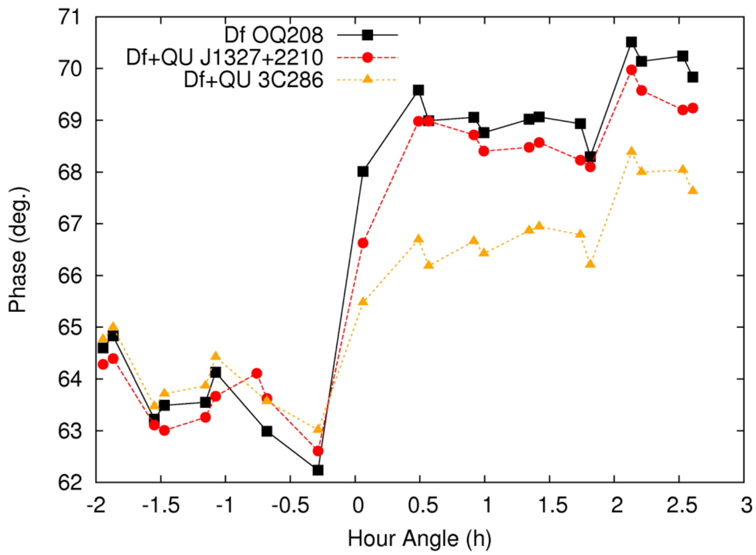

Figure 12: RL phase plotted against hour angle for 3C 286. The three curves represent derived RL phases using different strategies to derive the instrumental polarization. Data points labeled 'Df OQ208' was using the unpolarized calibrator OQ208 fitting only the instrumental polarization. Data points labeled 'Df+QU J1327+2210' and 'Df+QU 3C286' used respectively J1327+2210 a weakly polarized calibrator or 3C 286 solving for instrumental polarization while also solving for source polarization (QU-term). The data is based on the TSKY0001 observation at X band.

3.7 Reference Antennas

The RL phases were derived for a number of different reference antennas using the TSKY0001 dataset and choosing five innermost antennas (2, 4, 7, 24, and 25) as shown on the right in Fig. 13. This ensures that the observed RL phase variabilty is not introduced by the choice of a bad reference antenna. As can be seen in Fig. 13, **the choice of reference antenna makes no difference to the observed RL phase variation**.

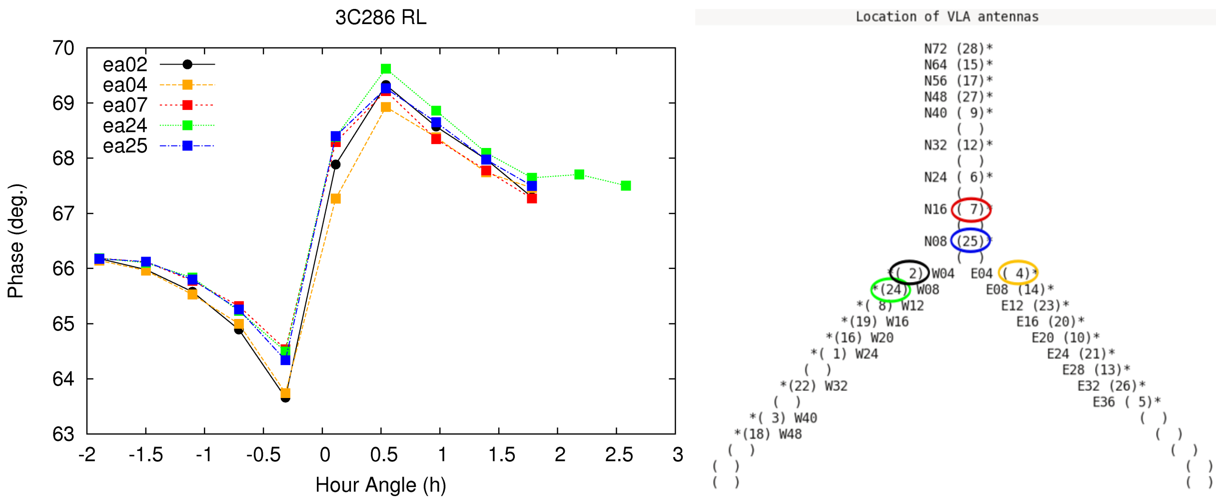

Figure 13: Left: RL phase plotted against hour angle for calibration with five different reference antennas (2, 4, 7, 24, and 25). Right: Location of the antennas chosen for calibration encircled with colored ellipses matching the colors of the data points in the left RL phase figure.

3.8 Baseline Dependence

In the following the baseline dependence of the RL phase variability of 3C 286 using the TCAL0004 A-array dataset is analyzed. In the above subsection the RL phase was derived averaging across the length of a scan, 128 MHz of the spectral window and across all baselines. In Fig. 14 the RL phase is plotted for all baselines against time only averaging across frequency and time. This reveals a huge spread in RL phase across time with the spread being larger before transit (50–80°) compared to after transit (60–80°). For comparison in the same Figure the RL phase variability for each channel is shown while averaging all baselines and across the length of each scan.

The spread in baselines is suspicous and is further investigated. A number of baselines forming triangles are selected based on their extreme spread in values. Fig. 15 to 19 show the RL phase plots for each of those baslines together with a visualization of the location of the antennas and the triangle the baselines form.

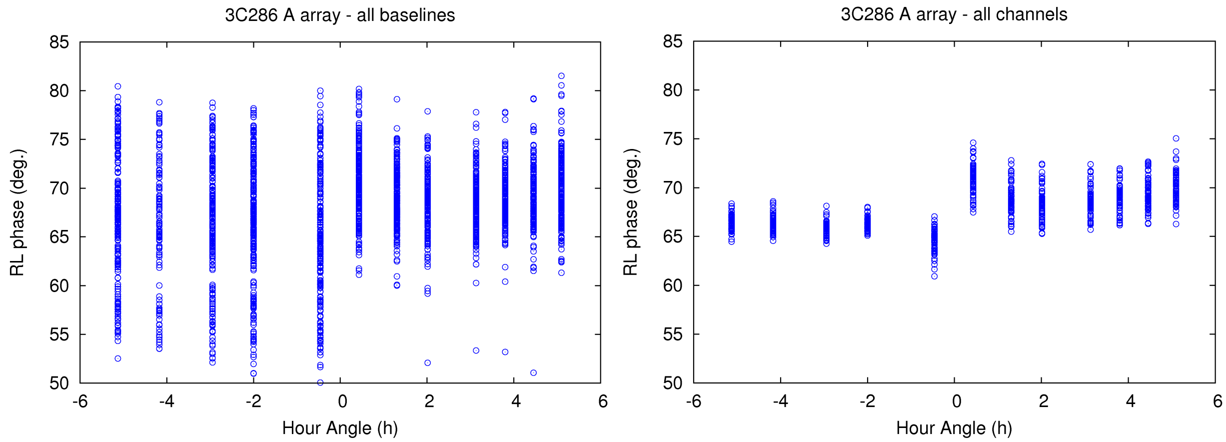

Figure 14: Left: RL phase variability for each baseline, only averaging across length of each scan and all channels within the spectral window. Right: RL phase variability for each channel within the selected spectral window, only averaging across length of each scan and all baselines.

- ea01–ea07–ea10 (Fig. 15): Two extreme baslines were picked and the closing baseline to form a triangle. In the case of this combination the closing baseline between ea01&ea07 does not show significant variability in RL phase, while baselines between ea07/ea01 and ea10 show significant offsets by more than 10° in RL phase before and after transit.

- ea01–ea05–ea07 (Fig. 16): Similar to the first triangle a different combination was chosen where the closing baseline ea01&ea07 shows little variabilty, while baselines to ea05 are diverging before transit and converge after transit with a spread of ∼10°.

- ea04–ea05–ea10 (Fig. 17): This case is again similar to the first triangle, however the closing baseline ea04&ea05 does show a jump in RL phase before and after transit.

- ea10–ea12–ea28 (Fig. 18): This triangle of very short baselines exhibit small offsets before and after transit, however around transit the RL phase spikes.

- ea03–ea06–ea09 (Fig. 19): The last triangle that is show cased here demonstrates the RL phase variability on long baselines, where again before transit a spread in RL phase of ∼10° is observed, while the post transit variability in RL phase is signifcantly smaller.

In summary, **individual baselines show similar but distinct RL phase variability** that do not clearly trace to issues with particular antennas. There is **no difference in variability observed with baseline length**, short as well as long baselines show spreads in RL variability of the order of ∼10° within a given triangle.

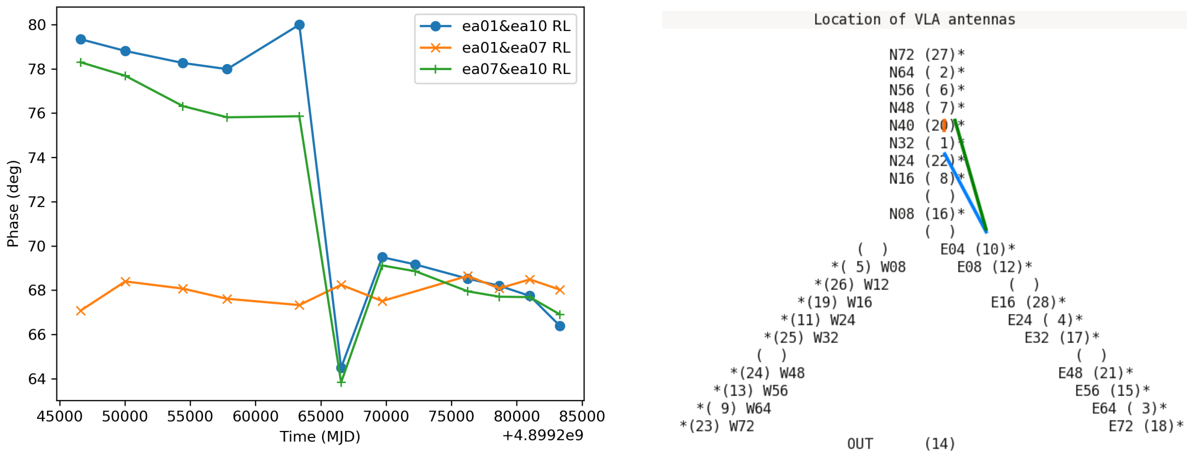

Figure 15: *Left*: Time variability of RL phase for the baselines ea01&ea10, ea01&ea07, and ea07&ea10. *Right*: Array configuration indicating the chosen baselines.

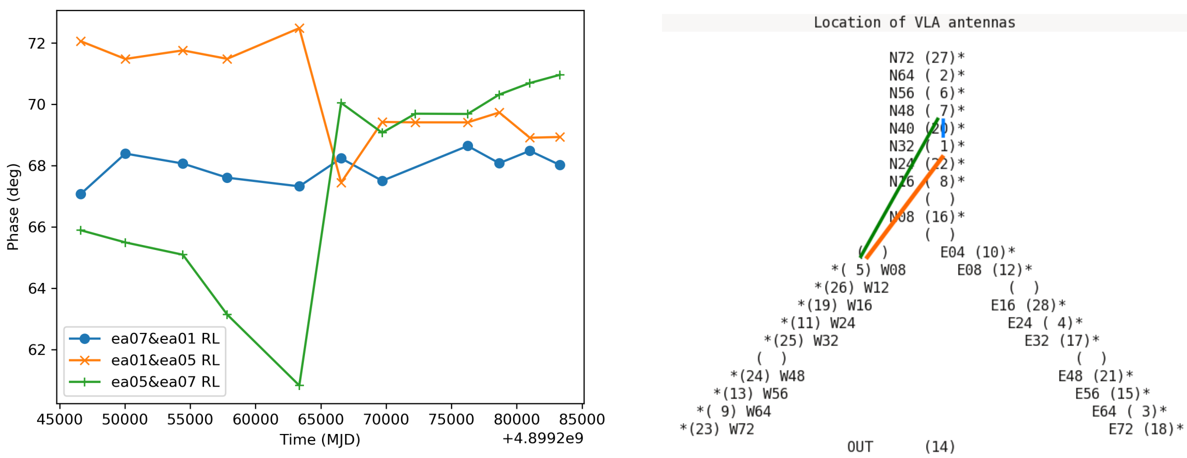

Figure 16: *Left*: Time variability of RL phase for the baselines ea07&ea01, ea01&ea05, and ea05&ea07. *Right*: Array configuration indicating the chosen baselines.

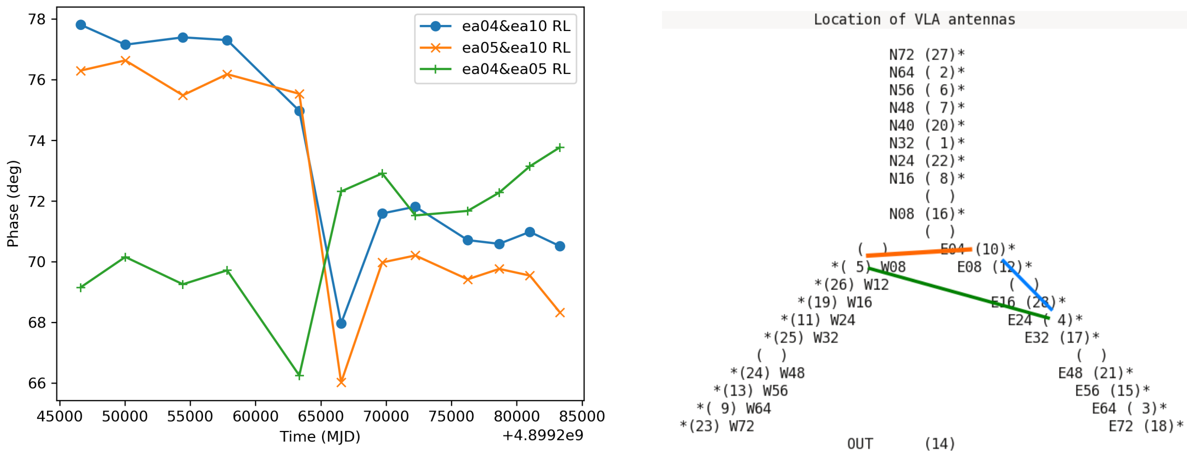

Figure 17: *Left*: Time variability of RL phase for the baselines ea04&ea10, ea05&ea10, and ea04&ea05. *Right*: Array configuration indicating the chosen baselines.

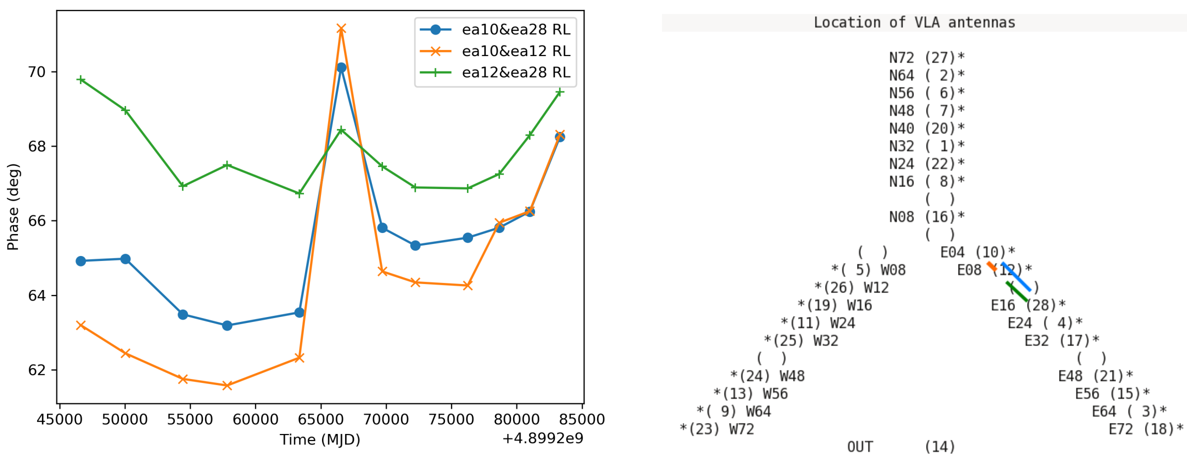

Figure 18: *Left*: Time variability of RL phase for the baselines ea10&ea28, ea10&ea12, and ea12&ea28. *Right*: Array configuration indicating the chosen baselines.

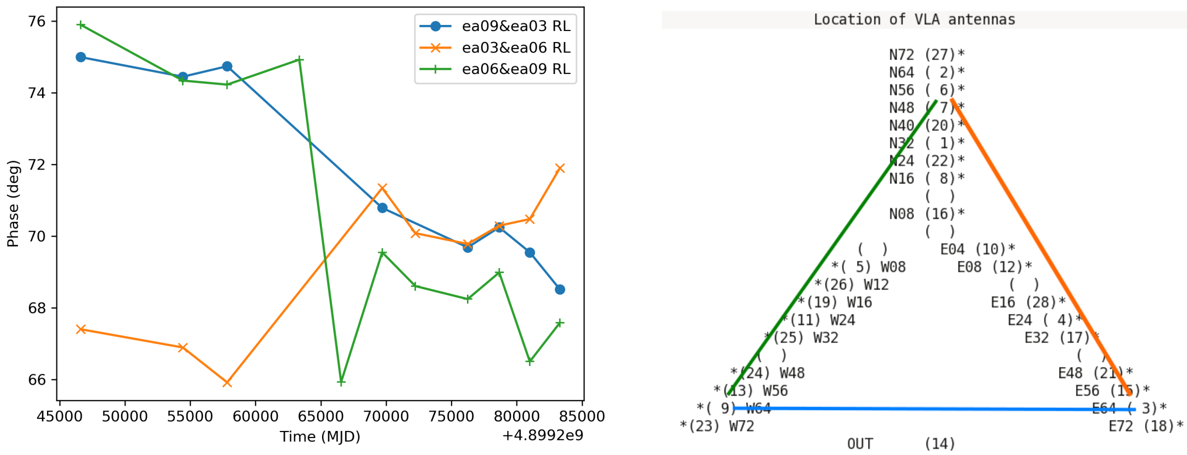

Figure 19: *Left*: Time variability of RL phase for the baselines ea09&ea03, ea03&ea06, and ea06&ea09. *Right*: Array configuration indicating the chosen baselines.

3.9 Delay Stability

Using the TSKY0001 dataset at X band the delay stability across the observation is investigated. To do so the AIPS task FRING is used to determine delays from a single scan on 3C 286. This prior delay solution is applied and FRING is rerun across all scans on 3C 286. The resulting delay solutions are then plotted subtracting the delay difference between the parallel hands (R-L), shown in Fig. 20, which indicate that delays are stable across the entire observation with ± 5 ps for all antennas.

3.10 Per Antenna Phase Stability

Using a similar approach to investigating the delay stability, the AIPS FRING per antenna R-L phase solutions can be plotted after applying delay and phase corrections based on a single scan of 3C 286. Fig. 21 plots the residual R-L phase differences against time for six select antennas that show the largest variability. Since all spectral windows are plotted one can see the phase changes with frequency across the lower baseband. The magnitude of which is typically less than $\sim 2^\circ$ in phase.

In the case of antennas 1, 6, and 12 there are dominant peaks around the time of transit. These correspond to antennas which are located at antenna pads that have the highest recorded pad tilts, which as a consequency tilt the antennas outside of the assumed single plane for which the parallactic angle is calculated for the array. Fig. 22 was produced by Rick Perley plotting the deviation in Parallactic Angle in degrees for different position offsets in latitude and longitude simulating a $\sim 0.2^\circ$ offset. The data suggest a latitude offset rather than one in longitude. However, the magnitude of the offset does not match the observed antenna tilts, thus the conclusion is that the observed RL phase variation

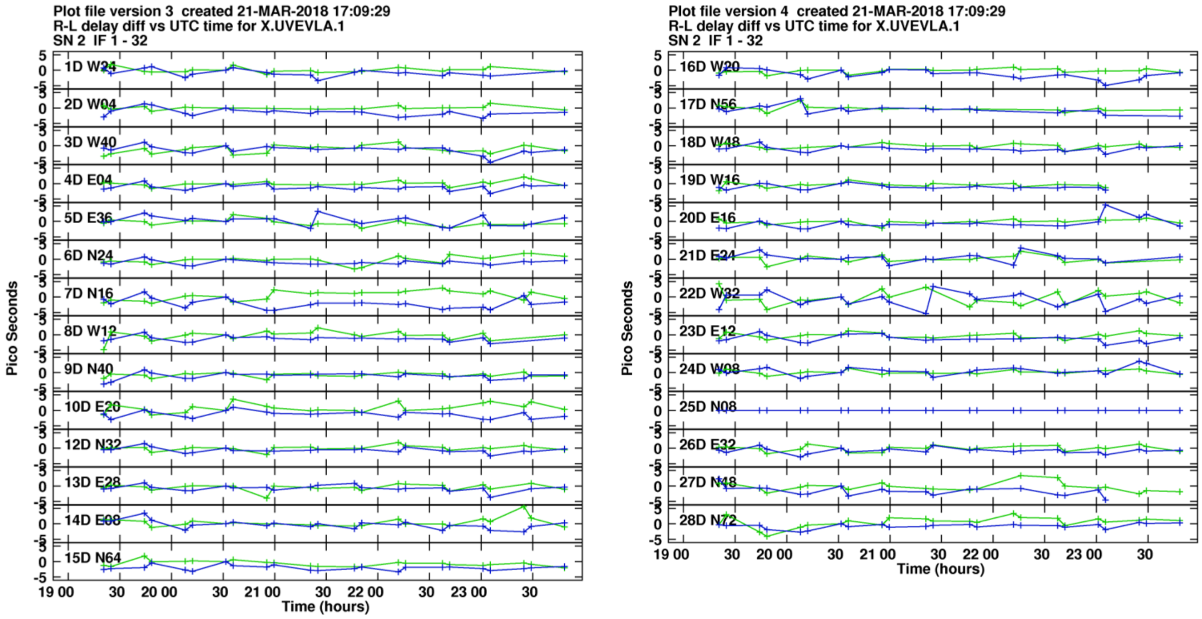

Figure 20: Residual R-L antenna based delays for all spectral windows (IF 1–32). The plot scale of the y-axis is fixed to ±5 pico seconds.

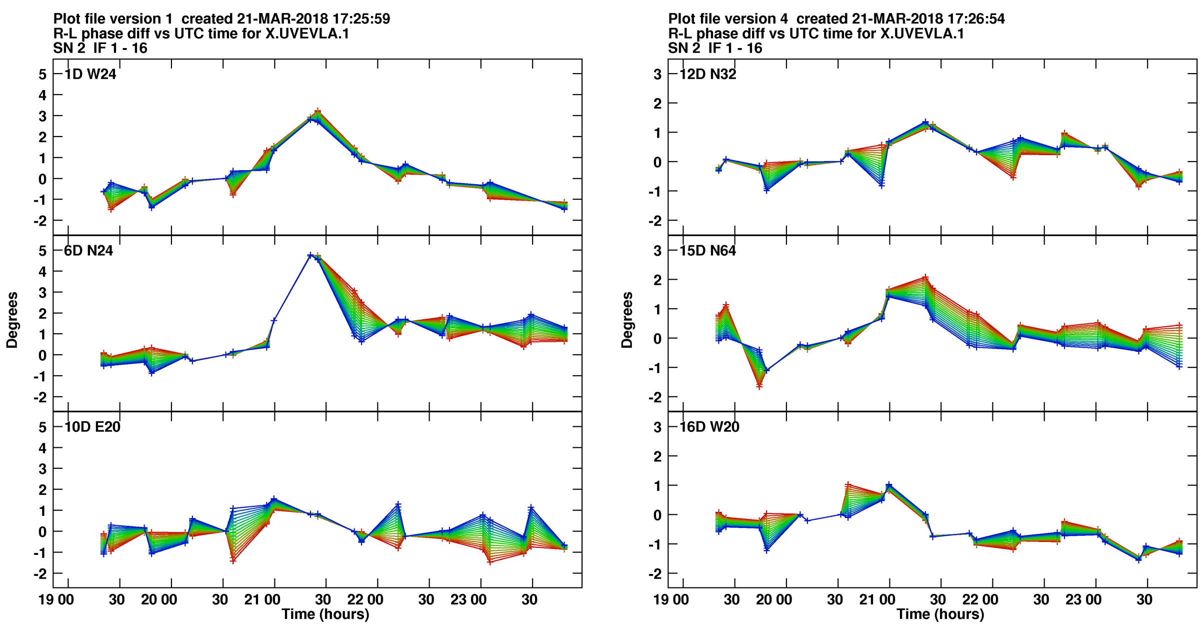

Figure 21: Residual R-L antenna based phase differences for all the lower baseband spectral windows (IF 1–16). The plot scale of the y-axis is not fixed to 5 – -2° for antennas 1, 6, and 10 and is fixed to 3– -2° for antennas 12, 15, and 16.

cannot be purely explained by antenna pad tilts.

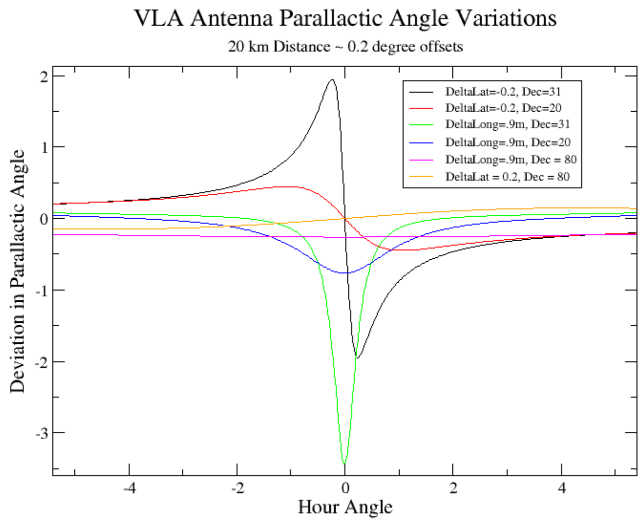

Figure 22: Deviation in parallactic angle for objects at different declinations for antenna position offsets in latitude and longitude corresponding to a 0.2° antenna tilt offset at 20 km distance. *Credit: Rick Perley*

4 Summary & Conclusions

This list summarizes the investigation into the cause of the observed RL phase variability. At this point all obvious causes are ruled out.

- Ruled out ionospheric Faraday rotation as the dominant cause of RL phase variability.
- No significant differences when calibrating with CASA or AIPS.
- A&B array configurations show similar phase variations; C array differs showing an elevation dependent RL phase.
- Similar RL phase variations observed between S and X bands.
- Polarized source structure does not affect calibration at the observed level of RL phase variability.
- Solving for instrumental polarization using an unpolarized as well as a polarized calibrator, thus not fitting and fitting additional source intrinsic polarization, does not change the observed RL phase variability.

- The choice of reference antennas makes no difference to the observed RL phase variability.
- Significant variability on RL phase is observed from baseline to baseline forming an overall spread of $\sim 30°$ in RL phase before transit and $\sim 20°$ after transit of 3C 286.
- The spread in RL phase within a given triangle of baselines is found to be $\sim 10°$ and seems independent of baseline lengths.
- There is no indication that individual antennas are responsible for the RL phase variability.
- The parallel hand delays can be assumed stable across an observation.

A dedicated one hour meeting was held at the DSOC in Socorro on March 22, 2018. In attendance were Bryan Butler, Barry Clark, Bill Cotton, Vivek Dhawan, Eric Greisen, Preshanth Jagannathan, George Moellenbrock, Rick Perley, and Frank Schinzel. The material in this document were presented and possible causes of the RL phase variability were discussed. Bill Cotton noted that he has seen a similar effect in his data before as well. Among the suggested causes of the RL phase variability were antenna tilts, geocentric vs. geodetic coordinate system for calculation of the parallactic angle, or annual and diurnal aberration effects that might have not been taken into account properly. The conclusion was that we seem to be dealing with a second order effect and that no individual suggested cause can produce RL phase variations of the observed magnitude. Given this situation and having not identified the cause of the apparent geometrical offsets, it cannot be assumed that absolute polarization angles across the sky can be determined to an absolute accuracy of better than ~ 4–$5°$. It is clear that significant effort is required to further investigate the cause of this issue in order to improve the absolute polarization angle accuracy of the EVLA.

References

[1] R.J. Sault and R. Perley. Polarimetric calibration and dynamic range issues. NRAO EVLA Memo 177, 2014.

[2] A.R. Thompson, J.M. Moran, and G.W. Swenson. *Interferometry and Synthesis in Radio Astronomy*. Wiley-VCH Verlag GmbH, 2015.

Revision History

Revision	**Date**	**Author(s)**	**Description**
1.0	2018-05-02	Frank Schinzel	Original